# Deformation and breakup of a viscoelastic drop in a Newtonian matrix under steady shear

## NISHITH AGGARWAL AND KAUSIK SARKAR

University of Delaware, Newark, USA

The deformation of a viscoelastic drop suspended in a Newtonian fluid subjected to a steady shear is investigated using a front-tracking finite-difference method. The viscoelasticity is modelled using the Oldroyd-B constitutive equation. The drop response with increasing relaxation time $\lambda$ and varying polymeric to the total drop viscosity ratio $\beta$ is studied and explained by examining the elastic and viscous stresses at the interface. Steady-state drop deformation was seen to decrease from its Newtonian value with increasing viscoelasticity. A slight non-monotonicity in steady-state deformation with increasing Deborah number is observed at high Capillary numbers. Transient drop deformation displays an overshoot before settling down to a lower value of deformation. The overshoot increases with increasing $\beta$. The drop shows slightly decreased alignment with the flow with increasing viscoelasticity. A simple ordinary differential equation model is developed to explain the various behaviours and the scalings observed numerically. The critical Capillary number for drop breakup is observed to increase with Deborah number owing to the inhibitive effects of viscoelasticity, the increase being linear for small Deborah number.

## 1. Introduction

Immiscible blends of liquids/polymers are of considerable importance because of their presence in, for example, foods, paints, cosmetics, and chemical and material processing. Macroscopic properties of these emulsions are directly related to the microstructure resulting from drop deformation, breakup and coalescence (Tucker & Moldenaers 2002; Li & Sarkar 2005b–d). In the case of a dilute emulsion with negligible drop–drop interactions, the dynamics of a single drop provides complete information about the emulsion behaviour. Accordingly, single drop breakup and deformation in simple linear flows have been extensively investigated since the pioneering study by Taylor (1932, 1934). Most of these investigations are restricted to systems where both component fluids are Newtonian (Sarkar & Schowalter 2001a, b; Li & Sarkar 2005a; for a review see Grace 1982; Rallison 1984; Stone 1994). Non-Newtonian components, however, can have significant effects on drop-deformation and breakup (Tucker & Moldenaers 2002; Yue *et al.* 2005a, b).

Drop deformation in a Newtonian system is governed by the Capillary number – ratio of the viscous stretching force to the resistive force due to interfacial tension – and viscosity ratio. Below a critical Capillary number, drops retain an elongated but bounded shape, whereas above it they break up. Viscoelasticity changes drop deformation as well as the critical Capillary number. The effects of viscoelasticity on drop deformation have primarily been attributed to normal stresses, although actually it is a composite result of changes in both viscous and viscoelastic stresses and the

flow modification (Ramaswamy & Leal 1999*a*, *b*; Yue *et al.* 2005*a*). Viscoelastic drop deformation has been shown to decrease as a result of the normal stresses in the drop phase. Gauthier, Goldsmith & Mason (1971), de Bruijn (1989) and Varanasi, Ryan and Stroeve (1994) found the critical capillary number $Ca_{cr}$ for viscoelastic drops in a Newtonian matrix to be higher than that in the corresponding Newtonian case owing to the hindering effects of drop phase normal stresses. Mighri *et al.* (1997, 1998), using constant-viscosity Boger fluids, observed the critical capillary numbers to increase with drop elasticity, but critical capillary numbers were found to decrease with increasing matrix viscoelasticity. However, Guido, Simeone & Greco (2003) and Sibillo, Simeone & Guido (2004) found that matrix viscoelasticity hinders breakup of a Newtonian drop in simple shear.

Greco (2002) obtained a perturbative solution to the single-drop problem for a second-order drop and matrix model, and compared it with experimental results for the deformation of a Newtonian drop in a viscoelastic matrix (Guido *et al.* 2003). Guido *et al.* (2003) found significant deviation from the Newtonian behaviour only in the drop orientation angle, and not in the deformation at small Capillary numbers. A phenomenological model by Maffetone & Greco (2004) that assumes an ellipsoidal drop shape, but otherwise allows large deformation, predicted a less deformed Newtonian drop in a viscoelastic matrix, as seen in the experiments by Guido *et al.* (2003).

Computational investigations of viscoelastic drop dynamics have been initiated using a number of different methodologies. Toose, Guerts & Kuerten (1995) used a boundary-integral method for simulating a two-dimensional linear Oldroyd-B drop in a Newtonian matrix, and concluded that for small deformation, drop viscoelasticity affects only the transient behaviour. Ramaswamy & Leal (1999*a*, *b*) and Hooper *et al.* (2001) used a finite-element method to investigate axisymmetric deformation of viscoelastic drops using FENE-CR and Oldroyd-B equations, respectively, in a uniaxial extension. They predicted reduced deformation for a viscoelastic drop in a viscous matrix and enhanced deformation in the opposite case. Pilapakkam & Singh (2004) presented finite-element simulations using an Oldroyd-B model. They observed a non-monotonic change in drop deformation for a viscoelastic drop subjected to shear in a Newtonian matrix. Matrix phase elasticity was, however, seen to increase drop deformation. Yue *et al.* (2005*a*, *b*) used a diffuse-interface method to study viscoelastic effects on two-dimensional drops in simple shear flows. In their study, they showed variations in stresses at the interface with drop/matrix elasticity to explain viscoelastic effects. They concluded that the drop viscoelasticity inhibits drop deformation, in conformity with previous observations. Matrix viscoelasticity, however, was shown to cause a non-monotonic change in drop deformation with increasing viscoelasticity. In a clear departure from these studies, Sarkar and Schowalter performed a two-dimensional investigation of viscous (Sarkar & Schowalter 2001*a*, *b*) and viscoelastic (Sarkar & Schowalter 2000) drop, deforming in time periodic extensional flows. They developed a new viscoelastic algorithm that offers a natural viscous/viscoelastic stress split (Perera & Walters 1977; Rajagopalan, Armstrong & Brown 1990; Sun & Tanner 1994; Sun, Phan-Thien & Tanner 1996) and implemented it into the front-tracking method. Apart from the time periodicity, the other distinctive aspect of this investigation was inclusion of inertia. At finite inertia, the resonance of the viscous system found by Sarkar & Schowalter (2001*a*, *b*) is significantly altered by the upper convective Maxwell viscoelasticity in that while the elasticity increases the effective spring term of the system, it decreases damping. As a result, the deformation could either increase or decrease with increasing viscoelasticity (Weissenberg number)
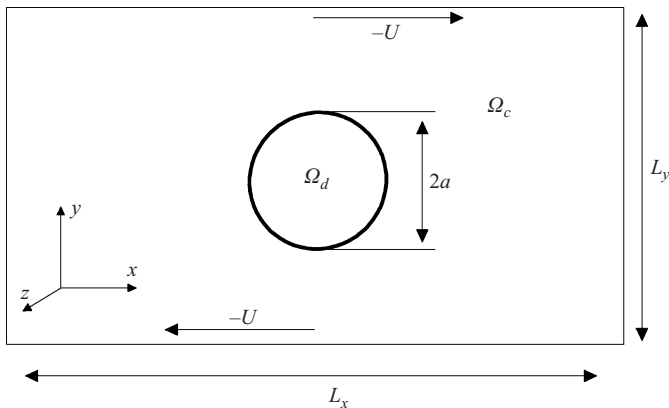
FIGURE 1. A schematic of the domain of calculation.

and frequency, depending upon other parameters. They developed a simple ordinary differential equation model to describe the observed behaviours. They also noted an additional effect of spatial resonance of shear waves within the drop boundary which leads to increased deformation at certain Weissenberg numbers. These studies are, however, limited by the two-dimensional nature of their computations. Khismatullin, Renardy & Renardy (2006) have implemented a three-dimensional volume-of-fluid method for investigation of the viscoelastic single-drop problem.

Here, we present a three-dimensional investigation of deformation and breakup of an Oldroyd-B drop in a Newtonian matrix at small Reynolds number ($Re = 0.1$). We choose Oldroyd-B as the simplest materially frame-indifferent constitutive equation with a single relaxation time; it has a shear-independent viscosity, and supports a positive first normal stress and a zero second normal stress in shear. We note that just like the upper convective Maxwell, Oldroyd-B is equivalent to an infinitely extensible elastic dumb-bell model. Such models predict an infinite extensional viscosity in a homogeneous steady uniaxial extension for $De = 0.5$. The present investigation of a drop in a shear flow did not encounter any of the associated problems (see however, Rallison & Hinch 1988). Note that the viscoelastic algorithm developed here can be used for other differential constitutive models, including those with finite extensibility such as FENE-CR. In §2, we provide the mathematical formulation of the problem. Section 3 describes the numerical implementation of the front-tracking method and the scheme for the viscoelastic phase. In §4, we provide an intuitive force balance model that is used later to explain the simulation results in §5. Section 6 summarizes the work.

## 2. Mathematical formulation

The flow of the droplet matrix system is governed by the momentum conservation equation:

$$\frac{\partial(\rho\boldsymbol{u})}{\partial t} + \nabla\cdot(\rho\boldsymbol{u}\boldsymbol{u}) = \nabla\cdot\boldsymbol{\tau} - \int_{\partial B} \mathrm{d}\boldsymbol{x}_B \kappa\boldsymbol{n}\Gamma\delta(\boldsymbol{x}-\boldsymbol{x}_B), \tag{1}$$

in the entire domain $\Omega$ (figure 1) consisting of the dispersed phase $\Omega_D$ and the continuous phase $\Omega_C$. Here, $\Gamma$ is the interfacial tension (constant), $\partial B$ represents the surface of the drop consisting of the points $\boldsymbol{x}_B$, $\kappa$ the local curvature, $\boldsymbol{n}$ the outward normal, and $\delta(\boldsymbol{x}-\boldsymbol{x}_B)$ is the three-dimensional Dirac delta function. We represent

the interfacial tension force as a singular body force in anticipation of the numerical (front-tracking) implementation. $\tau$ is the total stress tensor given by:

$$\tau = -p\boldsymbol{I} + \boldsymbol{T}^p + \boldsymbol{T}^v, \quad \boldsymbol{T}^v = \mu_s \boldsymbol{D}, \tag{2}$$

where $p$ is the pressure, $\mu_s$ is the solvent viscosity and $\boldsymbol{D} = (\nabla\boldsymbol{u}) + (\nabla\boldsymbol{u})^T$ is the strain rate tensor. $\boldsymbol{T}^p$ is the extra stress (also referred to as polymer stress or viscoelastic stress) due to the presence of the polymer. We use the Oldroyd-B constitutive equation for $\boldsymbol{T}^p$:

$$\lambda\overset{\nabla}{\boldsymbol{T}^p} + \boldsymbol{T}^p = \mu_p \boldsymbol{D}, \tag{3}$$

where $\mu_p$ is the polymeric viscosity, $\lambda$ is the relaxation time ($\lambda = 0$ in the Newtonian component outside), and $\overset{\nabla}{\boldsymbol{T}^p}$ is the upper convected time derivative defined as:

$$\overset{\nabla}{\boldsymbol{T}^p} = \frac{\partial \boldsymbol{T}^p}{\partial t} + \boldsymbol{u}\cdot\nabla\boldsymbol{T}^p - (\nabla\boldsymbol{u})\boldsymbol{T}^p - \boldsymbol{T}^p(\nabla\boldsymbol{u})^T. \tag{4}$$

The superscript $T$ represents the transpose. The fluid is considered to be incompressible in both phases:

$$\nabla\cdot\boldsymbol{u} = \boldsymbol{0}. \tag{5}$$

The Oldroyd-B fluid does not show shear thinning effects. Shear flow of an Oldroyd-B fluid gives rise to a first normal stress difference, $N_1 = 2\mu_p\dot{\gamma}^2\lambda$ and shear stress $T^p_{xy} = \mu_p\dot{\gamma}$ ($\dot{\gamma}$ is the shear).

## 3. Numerical implementation

The drop is placed in a computational domain (convergence with increasing domain size was verified). The flow is considered to be periodic in the $x$- and $z$- directions. Velocities are specified at the upper and lower plates in the $y$- direction to impose a simple shear of magnitude $\dot{\gamma}$. The matrix being Newtonian, the extra stresses are identically zero on the boundary of the computational domain. The initial velocity field is also assumed to be a simple shear, where a spherical drop of radius $a$ is suddenly introduced at $t = 0$. The extra stresses are assumed to be zero initially.

### 3.1. Front tracking method

We use a front-tracking finite-difference method (Unverdi & Tryggvason 1992; Tryggvason *et al.* 1998, 2001) to solve the initial-boundary-value problem. The method is discussed in detail in Sarkar & Schowalter (2000, 2001a) and Li & Sarkar (2005a). Here, we provide only a brief outline. The drop-matrix two-phase system with different properties (density, viscosity, relaxation time) across a sharp drop boundary is transformed into a single-phase system with properties varying smoothly over a few computational grid points (here $\sim 4\Delta x$). The system therefore has the same equation everywhere, e.g. the same Oldroyd-B equation for polymeric stresses even in the Newtonian phase outside, with relaxation time $\lambda = 0$ (Sarkar & Schowalter 2000). In front tracking, the smoothed representations of the properties are found by solving a Poisson's equation for the indicator function, which is zero outside and unity inside (Unverdi & Tryggvason 1992). Apart from a regular three-dimensional Cartesian grid in the entire domain, the moving interface (front) is separately discretized using triangular elements. The front is used in determining the properties. Once the smoothly varying property fields are attained, (1) is solved by a finite-difference method to obtain the velocities at the Cartesian grid points. The interface evolution is described by the nodal (triangle vertices) velocity on the

front obtained by interpolation. For this interpolation as well as those involved in representing the singular terms in the Poisson's equation and in (1) due to the surface tension, a smoothed surrogate of delta function (Peskin 1977) is used. An adaptive regridding scheme is used to prevent excessive distortion of the front elements.

### 3.2. *Finite difference*

The momentum equation is solved on a regular staggered grid with velocity nodes at the face centres and pressure and material properties defined at the cell centres. The extra stress nodes are also placed in a staggered arrangement, with normal stress $T_{xx}^p$, $T_{yy}^p$ and $T_{zz}^p$ nodes at cell centres and shear stress $T_{xy}^p$, $T_{yz}^p$ and $T_{zx}^p$ nodes at cell corners. The momentum equation (1) is solved by an operator splitting projection method in two steps:

$$\frac{\rho^{n+1}\boldsymbol{u}^* - (\rho\boldsymbol{u})^n}{\Delta t} = -\nabla\cdot(\rho\boldsymbol{u}\boldsymbol{u})^n + \boldsymbol{F}^n + \nabla\cdot\boldsymbol{\tau}^n, \tag{6}$$

$$\frac{\boldsymbol{u}^{n+1} - \boldsymbol{u}^*}{\Delta t} = -\frac{1}{\rho^{n+1}}\nabla p^{n+1}, \quad \nabla\cdot\left(\frac{1}{\nabla\rho^{n+1}}p^{n+1}\right) = \frac{1}{\Delta t}\nabla\cdot\boldsymbol{u}^*, \tag{7}$$

$\boldsymbol{u}^*$ is an intermediate velocity. $\boldsymbol{F}^n$ is the body force, which in our case of neutrally buoyant drops comprises only the surface tension force. The Poisson equation for pressure is solved using a multi-grid method.

### 3.3. *Constitutive equation*

The Oldroyd-B constitutive equation for extra stress can be expressed as:

$$\lambda\frac{\partial\boldsymbol{T}^p}{\partial t} + \boldsymbol{T}^p = \boldsymbol{K}(t), \tag{8}$$

where,

$$\boldsymbol{K}(t) = \mu_p\boldsymbol{D} - \lambda\{\boldsymbol{u}\cdot\nabla\boldsymbol{T}^p - (\nabla\boldsymbol{u})\boldsymbol{T}^p - \boldsymbol{T}^p(\nabla\boldsymbol{u})^T\}. \tag{9}$$

A simple explicit scheme in time would give:

$$\frac{(\boldsymbol{T}^p)^{n+1} - (\boldsymbol{T}^p)^n}{\Delta t} = \frac{1}{\lambda}\{-\boldsymbol{T}^p + \mu_p\boldsymbol{D} - \lambda(\boldsymbol{u}\cdot\nabla\boldsymbol{T}^p - (\nabla\boldsymbol{u})\boldsymbol{T}^p - \boldsymbol{T}^p(\nabla\boldsymbol{u})^T)\}^n, \tag{10}$$

which for a Newtonian phase ($\lambda = 0$) would yield a scheme that is singular. Such a scheme cannot be used with a front-tracking method which uses a single equation for the entire computational domain. Sarkar & Schowalter (2000) suggested a new consistent scheme:

$$\boldsymbol{T}^p(t_n + \Delta t) - \boldsymbol{T}^p(t_n)\exp(-(\Delta t/\lambda))$$

$$= \boldsymbol{K}(t_n + \Delta t) - \boldsymbol{K}(t_n)\exp(-(t_n + \Delta t/\lambda)) + \int_{t_n}^{t_n+\Delta t}\exp(t/\lambda)\frac{\partial\boldsymbol{K}}{\partial t}\,\mathrm{d}t. \tag{11}$$

Neglecting the integral and assuming $\boldsymbol{K}(t_n + \Delta t) \simeq \boldsymbol{K}(t_n)$, we obtain the difference scheme:

$$(\boldsymbol{T}^p)^{n+1} = (\boldsymbol{T}^p)^n\exp(-(\Delta t/\lambda)) + \boldsymbol{K}^n(1 - \exp(-(\Delta t/\lambda))). \tag{12}$$

Note that the above scheme is consistent in the limit of $\lambda \to 0$. We could choose $\boldsymbol{K}^{n+1}$ for the right-hand side to arrive at an implicit scheme. Also note an automatic splitting of the viscous and elastic extra stresses:

$$(\boldsymbol{T}^p)^{n+1} = \mu_p\boldsymbol{D}^n + \left[(\boldsymbol{T}^p)^n - \mu_p\boldsymbol{D}^n\right]\exp(-(\Delta t/\lambda)) + \left(\boldsymbol{K}^n - \mu_p\boldsymbol{D}^n\right)(1 - \exp(-(\Delta t/\lambda))), \tag{13}$$

the first term being the viscous contribution from the polymeric stress. Additional details can be found in Sarkar & Schowalter (2000).

### 3.4. ADI for viscous terms

An explicit scheme for calculating the viscous term suffers from restrictions on time steps, i.e. $\Delta t < 0.125(\Delta x)^2 \rho / \mu$, for low Reynolds numbers. To overcome this restriction, we treat some of the diffusive terms implicitly in alternate spatial directions (ADI). The viscous terms from (2) and (13) can be collected together as

$$\nabla \cdot \{(\mu_p + \mu_s)\boldsymbol{D}^n\} = D_{xy} + D_{yz} + D_{zx} + D_{zz} + D_{yy} + D_{xx}, \qquad (14)$$

where $D_{xy}, D_{yz}, D_{zx}$ are the mixed derivatives, and are computed by an explicit scheme. $D_{xx}, D_{yy}, D_{zz}$ are the double derivatives to be treated implicitly. We split the predictor step further and treat the diffusive terms by ADI:

$$
\left.
\begin{aligned}
\frac{\rho^{n+1}\boldsymbol{u}^{****} - (\rho\boldsymbol{u})^n}{\Delta t} &= -\nabla \cdot (\rho \boldsymbol{u}\boldsymbol{u})^n + \boldsymbol{F}^n + \nabla \cdot \left(\boldsymbol{T}_p^n - \mu_p \boldsymbol{D}^n\right) \\
&\quad + D_{xy}(\boldsymbol{u})^n + D_{yz}(\boldsymbol{u}^n) + D_{zx}(\boldsymbol{u}^n), \\
\rho^{n+1}\left(\frac{\boldsymbol{u}^{***} - \boldsymbol{u}^{****}}{\Delta t}\right) &= D_{zz}(\boldsymbol{u}^{***}), \quad \rho^{n+1}\left(\frac{\boldsymbol{u}^{**} - \boldsymbol{u}^{***}}{\Delta t}\right) = D_{yy}(\boldsymbol{u}^{**}), \\
\rho^{n+1}\left(\frac{\boldsymbol{u}^{*} - \boldsymbol{u}^{**}}{\Delta t}\right) &= D_{xx}(\boldsymbol{u}^{*}).
\end{aligned}
\right\}
\qquad (15)
$$

Each implicit equation above gives rise to a tri-diagonal system that is directly solved without iteration. The convergence of the scheme is ensured by prescribing for the intermediate velocities at the boundary $\partial \Omega$ as:

$$\boldsymbol{u}^* = \boldsymbol{u}^{**} = \boldsymbol{u}^{***} = \boldsymbol{u}^{****} = \boldsymbol{u}^{n+1}. \qquad (16)$$

The ADI scheme reduces the time step by one order of magnitude. We also adhere to other criteria $\Delta t < 2.0\mu/(\rho U_{max}^2)$ and $\Delta t < \Delta x / U_{max}$ at high Reynolds numbers to ensure the overall convergence of our simulations.

## 4. An ODE model for drop deformation

Sarkar & Schowalter (2001a) constructed a simple ordinary differential equation model to describe the essential physics of the drop deformation problem for the viscous case. They extended it for viscoelastic drops subjected to a time periodic flow by including a complex viscosity and explained the observed trends from their numerical simulation (Sarkar & Schowalter 2000). Here, we present a similar model to explain viscoelastic drop deformation in steady shear. The drop response (deformation) at zero inertia can be modelled by considering a balance of the viscous, interfacial and viscoelastic forces as:

$$\hat{\mu}\hat{a}^2 \dot{X} + \hat{\sigma}\hat{a}X + \hat{N}_1^d \hat{a}^2 X = \hat{\mu}\hat{a}^2 G_o, \quad X(0) = 0, \qquad (17)$$

where $X$ is representative of the non-dimensional drop deformation. The initial condition $X(0) = 0$ represents an initially undeformed drop. The term $\hat{\mu}\hat{a}^2 G_o$ is the 'forcing term' – viscous stretching force due to the applied shear $G_o$. The model material properties and drop radius are denoted with the same symbols used elsewhere in the paper, but with a hat. Each of the terms on the left-hand side represents a stress acting on an area $a^2$. The first term is representative of the viscous 'damping' which shows the other role besides stretching, that viscosity plays in this problem. The second term represents the interfacial contribution $\Delta\hat{p} \sim \hat{\sigma}/[\hat{a}(1+X)] \approx \hat{\sigma}(1-X)/\hat{a}$ ($\hat{\sigma}/\hat{a}$ just

gives rise to an isotropic pressure). The third term is the first normal stress contribution $\hat{N}_1^d$ arising from the tension along curved streamlines within the drop trying to snap back. To model this effect, we note that for an Oldroyd-B fluid in simple shear, the transient first normal stress difference is given as $N_1(t) = 2\mu_p\dot{\gamma}^2\lambda\{1 - \exp(-t/\lambda)(1 + t/\lambda)\}$ and the transient shear stress is given as $T_{xy}(t) = \mu_p\dot{\gamma}(1 - \exp(-t/\lambda))$. We use this value of $N_1(t)$ to represent the $\hat{N}_1^d$ in (17) However, a modification of the first term on the left-hand side of (17) to model the effect of the exponential growth of the polymeric shear stress inside the drop, does not affect the solution significantly. On non-dimensionalizing with length scale $\hat{a}$ time scale $G_o^{-1}$ and substituting for $\hat{N}_1^d$, we obtain

$$\frac{\mathrm{d}X}{\mathrm{d}t} + \{\hat{k} + \hat{\beta}\hat{D}e(1 - \exp(-t/\hat{D}e)(1 + t/\hat{D}e))\}X = 1, \qquad (18)$$

where $\hat{k} = \hat{\sigma}/\hat{\mu}\hat{a}G_o = \hat{C}a^{-1}$ is the inverse model Capillary number, $\hat{D}e = \hat{\lambda}G_o$ is the model Deborah number and $\hat{\beta} = \hat{\mu}_p/\hat{\mu}$ is the ratio of the polymeric viscosity to the total viscosity. For $\hat{D}e = 0$, we obtain the solution $X = \hat{C}a(1 - \exp(-t/\hat{C}a))$ from (18) in conformity with small deformation analytical results (Torza, Cox & Mason 1972). The steady-state deformation according to the above model is:

$$X = \frac{1}{\left(\hat{k} + \hat{\beta}\hat{D}e\right)} = \frac{\hat{C}a}{(1 + \hat{\beta}\hat{D}e\hat{C}a)}. \qquad (19)$$

The ODE model predicts that at steady-state drop deformation $D \propto \beta De Ca^2$ at first order in $De$. It is important to note that our model is only qualitative in that it presents only the dominant balance between the forces that are of the same order. However, their actual magnitudes are not represented. Therefore, rather than the actual deformation values, only the trend and scalings can be predicted by the model.

## 5. Results and discussion

We place a spherical drop of radius $a$ in a computational domain of size $L_x = 10a$, $L_y = 10a$ and $L_z = 5a$ (see figure 1). We impose velocities $U$ and $-U$, respectively, at the upper and lower plates to obtain a strain rate $\dot{\gamma} = 2U/L_y$. We use $a$ and $\dot{\gamma}^{-1}$ as length and the time scales to define the various non-dimensional parameters governing the problem: Reynolds number $Re = \rho_m a^2\dot{\gamma}/\mu_m$, capillary number $Ca = \mu_m a\dot{\gamma}/\Gamma$, Deborah number $De = \lambda\dot{\gamma}$, viscosity ratio $\lambda_\mu = \mu_d/\mu_m$, density ratio $\lambda_\rho = \rho_d/\rho_m$ and $\beta = \mu_{pd}/\mu_d$ – the ratio of the polymeric to the total drop viscosity. Subscripts $m$ and $d$ correspond to the matrix and the dispersed phase, respectively. For brevity, we restrict ourselves to cases with $\lambda_\rho = \lambda_\mu = 1$. The total dispersed phase viscosity is given as $\mu_d = \mu_{sd} + \mu_{pd}$, sum of the solvent and polymeric viscosities. We fix $Re = 0.1$, representing a low-Reynolds-number case. The explicit numerical method adopted here cannot simulate a Stokes flow. The governing non-dimensional parameters for the problem are then $Ca$, $De$ and $\beta$. We have fixed $\beta = 0.5$ for all our results, except in a later section where we specifically investigate the effects of $\beta$ variation.

### 5.1. Convergence study

Taylor (1932, 1934) observed that a bounded drop assumes an approximately ellipsoidal shape in a linear flow with a major and a minor axis of length $L$ and $B$; he defined the deformation by a measure $D = (L - B)/(L + B)$. In figure 2, we present a convergence study of our method with grid refinement; the time evolution of the deformation parameter $D$ is plotted for $Ca = 0.1$ and $De = 2.0$ for varying
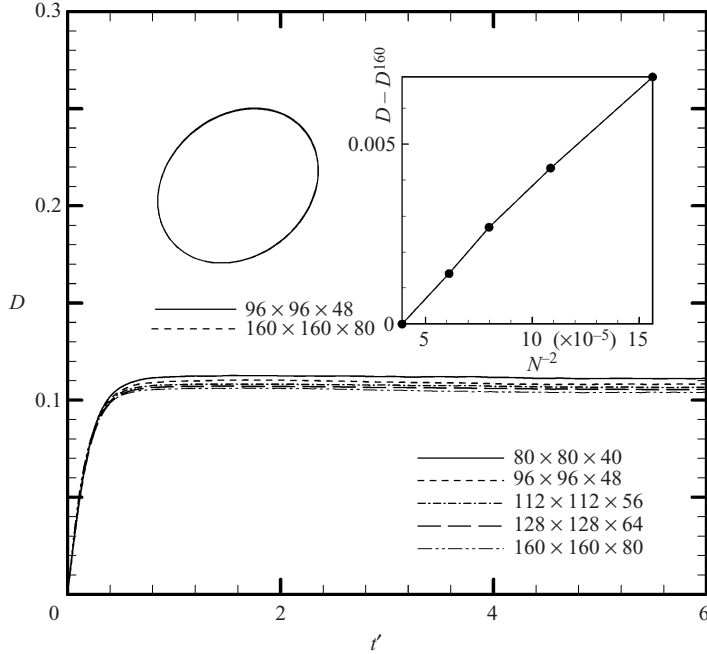
FIGURE 2. Convergence study of deformation $D$ plotted against non-dimensional time $t'(= \dot{\gamma}t)$ with varying grid discretization for $Re = 0.1$, $Ca = 0.1$ and $De = 2.0$; Insets show (*a*) convergence of drop shape (the two contours coincide) with resolution and (*b*) the error in $D$ (at steady state) with resolution $N$, where $N$ is the number of grid points along one of the coordinate directions. The error is computed with reference to the $D$ value at $160 \times 160 \times 80$.

grid resolution. We have increased the discretization level from $80 \times 80 \times 40$ up to a maximum of $160 \times 160 \times 80$. We see that $D$ increases as the drop deforms from its initial spherical shape and reaches a steady value $D_{st}$ in the long-time limit. $D$ decreases with increased discretization. $D_{st}$ plotted in the inset displays a quadratic convergence with discretization. We choose a $96 \times 96 \times 48$ grid for our computations. Even though we notice a slight deviation from the converged value at this discretization, we note that the actual drop shape does not vary much from the one with $160 \times 160 \times 80$ discretization, as also shown in the inset. We also investigated the effect of the size of the computational domain by increasing each dimension to 1.5 times the above mentioned lengths, and found $\sim 1\%$ variation in $D_{st}$ and no difference in drop shape. For determination of breakup parameters (presented later in this section) we use a larger domain with increased length in the $x$-direction $L_x/a = 15$ with the same grid spacing.

### 5.2. *Transient drop deformation*

In figure 3*a*, we plot the three axes of the drop as a function of time for $Ca = 0.2$ and varying $De$. They deviate from their initial value of unity; as in the Newtonian case, the drop elongates in one direction ($L$) and shortens in the other two directions ($B$ and $W$). The steady-state value of $L$ decreases, and $B$ and $W$ ($W$ is the ellipsoidal axis in the vorticity direction) increases with increasing $De$ owing to increased viscoelastic stresses inhibiting the drop deformation. Correspondingly, in figure 3*b*, long-time $D$ ($D_{st}$) shows a decrease with increasing $De$. For larger values of $De$ (approximately $De \geqslant 0.8$ for $Ca = 0.2$) we also note an overshoot in the transient deformation. This
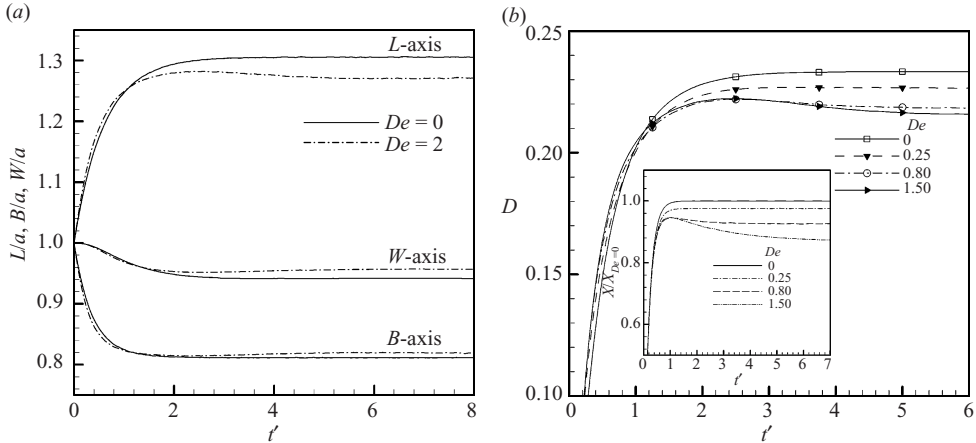
FIGURE 3. Effect of Deborah Number $De$ on drop deformation for $Ca = 0.2$ (*a*) Drop axes normalized with initial drop radius $a$ *vs.* non-dimensional time $t'$. (*b*) $D$ *vs.* $t'$. The Inset in (*b*) shows drop response $X$ predictions from our ODE model for $\hat{C}a = 0.2$.

can be explained by noting that the relaxation time associated with the Oldroyd-B constitutive equation leads to a finite time interval for the development of the (inhibitive) viscoelastic stresses which then decrease the drop deformation. Such an overshoot has also been reported by Yue *et al.* (2005*b*) for viscoelastic drops with $De/Ca > 5$ in their two-dimensional study. We also plot in the inset of figure 3*b*, the prediction of our ODE model. Note that as pointed out before, the model is not designed to be quantitative. The model results clearly predict the overshoot for sufficiently high $De$, as was seen in the numerical solution, indicating that the model truly represents the underlying physics. It should be noted that the overshoot in deformation is over the long-time steady value and not over the Newtonian value.

Yu *et al.* (2004) and Toose *et al.* (1995) have shown that for a linear viscoelastic system, the steady-state drop deformation value is the same as that for a Newtonian case. In contrast, the decrease in the steady-state deformation with increased $De$ observed here is a result of the nonlinear nature of the Oldroyd-B equation which gives rise to a finite first normal stress difference.

### 5.3. *Steady state drop deformation*

From the Newtonian study, we know that for $Ca < Ca_{cr}$, steady ellipsoidal drop shapes are obtained in the long-time limit. In figure 4(*a*), $D_{st}$ plotted as a function of $Ca$ shows a linear ($D_{st} \sim Ca$) variation for small $Ca$, similar to the Newtonian case (Taylor 1932). Consistent with figure 3(*b*), $D_{st}$ decreases with $De$. This effect is especially prominent for larger $Ca$ when the drop deformation is significant. In figure 4(*b*) we plot $D_{st}$ (normalized by its Newtonian $De = 0$ value) as a function of $De$ for various $Ca$. For comparison, we also plot the predictions of the ellipsoidal drop model given by Maffetone & Greco (2004). We obtain them by numerically solving their tensorial evolution equation to a steady state. Our results match well with predictions, at least up to $De \sim 0.5$ (for $Ca \lesssim 0.3$). At higher $De$, we see a saturation in $D_{st}$ i.e. we encounter a maximal contribution of the drop phase elasticity in inhibiting drop deformation. A similar saturation effect with increasing drop elasticity was observed by Mighri *et al.* (1998) in their determination of the critical capillary numbers for shear flow. The Maffetone & Greco (2004) model predicts a continued reduction
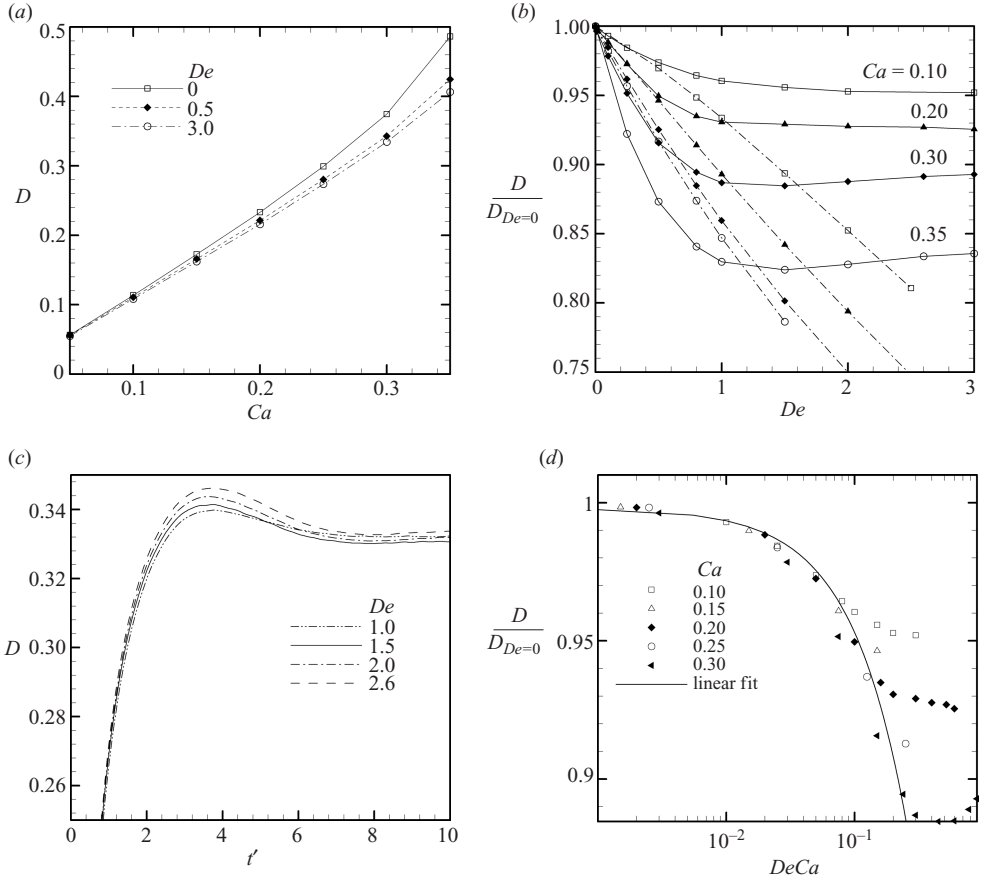
FIGURE 4. (*a*) Steady-state deformation $D_{st}$ *vs.* $Ca$ for different $De$. (*b*) Steady-state drop deformation $D$ (normalized with $D$ at $De=0$) *vs.* $De$ for different $Ca$ ($\square$, $Ca=0.1$; $\blacktriangle$, $Ca=0.2$; $\blacklozenge$, $Ca=0.3$; $\circ$, $Ca=0.35$) Solid lines represent our results. Dashed lines represent analytical results from Maffetone & Greco (2004). (*c*) $D$ *vs.* non-dimensional time $t'$ for $Ca=0.3$. (*d*) $D_{st}$ (normalized with $D$ at $De=0$) plotted *vs.* parameter $De\,Ca$ (in log scale) following the ODE model prediction $D/D_{De=0}\sim De\,Ca$. The solid line represents a least-squares fit through the data points. Note that data points for $Ca=0.3$ are not included in the determination of the fitting curve.

in drop deformation. Note that their results hold only for $\overline{De}=De/Ca\sim O(1)$. At a larger capillary number ($Ca=0.35$), our prediction differs significantly from the prediction of Maffetone & Greco's (2004) phenomenological model. Note that their model is formulated to match results from second-order perturbation theory only.

For large $Ca$ values ($Ca=0.3$ and $Ca=0.35$), we see a non-monotonicity – a slight increase in $D_{st}$ for larger $De$ in figure 4(*b*). To explore this small increase in $D_{st}$, we plot in figure 4(*c*) the transient deformation for $Ca=0.3$ and varying Deborah number. On increasing the Deborah number from 1.0 to 1.5, even though the initial deformation is higher, the long-time steady deformation decreases. However, on further increasing it to $De=2.0$ and $De=2.6$, the initial transient deformation is sufficiently high (owing to a lag in the development of viscoelastic stresses inside the drop) that the steady-state deformation settles to a higher value. Such non-monotonic behaviour of the $D_{st}\sim De$ curve has been previously observed by Pilapakkam &

Singh (2004). Yue *et al.* (2005) also commented that such behaviour was possible at high $Ca$. Note that the non-monotonic behaviour in $D_{st} \sim De$ is nonlinear in nature and therefore not captured by the ODE model, indicating its limitation.

We would like to point out that the observed reduction in drop deformation with $De$ owing to viscoelastic stresses is rather small ($\sim 10\%$ for $De = 3$ at $Ca = 0.3$), at least for the $Ca$ values considered in figure 4(*b*). The effect of viscoelasticity is dependent on the kinematics of the flow. The flow inside a bound ellipsoidal drop is essentially rotational, which may explain the relatively small effect of viscoelasticity. The flow field inside a viscoelastic drop does not deviate significantly from the purely Newtonian case. However, for $Ca$ close to the critical capillary number $Ca_{cr}$, the drop undergoes significant deformation and we expect viscoelasticity to play a significant role there. We explore this regime in a later section of this paper.

Our force balance model (19) predicts that the drop deformation for the Oldroyd-B drop/Newtonian matrix system at second order in $Ca$ and first order in $De$ is $X \propto \hat{Ca}(1 - \hat{\beta}\,\hat{De}\hat{Ca})$. Note that $D_{De=0} \sim Ca$. In figure 4(*c*) we plot the predictions of the model (linear fit; we have used data points in the small $Ca$ and $De$ range $Ca < 0.3$ and $De \leqslant 0.8$). We see that the prediction compares very well with the simulation data for small $Ca$ and $De$. We note that Greco's (2002) perturbative analysis using a second-order fluid predicts that deformation does not have an $O(Ca^2)$ term for either viscous or viscoelastic drops. The result is at variance with our simulation as well as earlier perturbative results of Barthès-Biesel & Acrivos 1973, Rallison (1984) and Bentley & Leal (1986); they all predict an $O(Ca^2)$ term for the deformation of a viscous drop. A careful reading of Greco (2002) reveals that it predicts both $L$ and $B$ to have identical dependence on $Ca^2$, cancelling such a term in deformation. Maffetone & Greco's (2004) phenomenological model compares better with experiment than Greco's second-order model. Our simulation matches the model predictions of Maffetone & Greco (figure 4*b*). We believe that the absence of the $Ca^2$ term in Greco (2002) for $D$ is a result of the assumptions underlying the perturbation analysis. Finally, we note that the deviation from the corresponding Newtonian problem occurring at second order in $Ca$ suggests that for $Ca \sim Ca_{cr}$, viscoelastic effects could be more pronounced.

In figure 5, we plot the deviation of the drop inclination angle $\varphi$ from the principal strain axis ($45°$) as a function of $De$. We see that a viscoelastic drop shows decreased alignment with the flow on increasing $De$. The drop inclination angle at $O(Ca^2)$ for the Newtonian case is given by:

$$\varphi = \frac{\pi}{4} - \frac{(2\lambda_\mu + 3)(19\lambda_\mu + 16)}{80(\lambda_\mu + 1)}Ca \qquad (20)$$

(Chaffey & Brenner 1967; Maffetone & Minale 1998). Our numerical predictions for $De = 0$ (shown in figures) match this analytical result. In the viscous case, drop deformation increases with $Ca$, and the deformed drop is increasingly aligned with the flow. Because of the decrease in deformation for a viscoelastic drop with increasing $De$, the drop becomes less inclined with the flow direction.

To further explain the observed inhibition of drop deformation with increasing $De$, following Yue *et al.* (2005*a*), we plot viscous and viscoelastic stresses along the circumference of the drop (in the central plane of the drop) as a function of the angular position $\phi$ from the flow direction. In figures 6(*a*) and 6(*b*), we plot the components of viscous and viscoelastic stresses normal to the interface, i.e. $T_{nn} = \boldsymbol{n} \cdot \boldsymbol{T} \cdot \boldsymbol{n}$, where $\boldsymbol{n}$ is the normal to the drop interface. In the Newtonian limit ($De \to 0$), the extra stress becomes $\mu_p \boldsymbol{D}$ (see (3)). We observe that the viscous normal stress $T_{nn}^v$ does not change significantly with $De$, either in magnitude or in trend. The peak value seems to shift
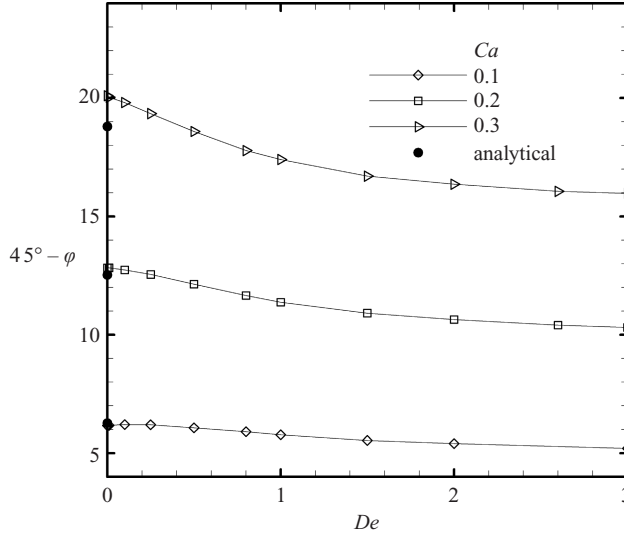
FIGURE 5. Deviation of steady state drop inclination angle $\varphi$ from strain-rate axis i.e. $45° - \varphi$ vs. *De* for different Capillary numbers. ●, the analytical predictions from (20).

towards higher angular positions owing to an increase in the overall drop inclination angle (figure 5). The viscoelastic normal stress $T_{nn}^p$, however, shows a marked increase in its peak value with increasing *De*. We also see a consistent shift of the peak values towards lower angular positions with increasing *De*. The viscoelastic normal stresses are tensile and maximum around the drop tip, hence exerting an inward pull, which reduces the *L*-axis deformation. This stress is, however, weakly compressive at the drop equator and hence exerts a 'push' which decreases the *B*-axis deformation.

In figure 7(*a*), streamlines for $Ca = 0.2$ $De = 2.0$ are plotted. A fluid element close to the interface is going around the circumference of the drop. Note that the 'instantaneous' viscous stresses are representative of the strain rate. Increasing *De* implies a higher relaxation time for the fluid element and hence, in a steady flow, there is an increased time lag between the maximum strain rate and the maximum viscoelastic stress. Indeed, this explains why the viscoelastic stress peaks show an angular shift relative to the viscous stress peaks (figure 6*b*). We will return to this explanation later in the paper when we discuss the effects of varying $\beta$. The nonlinearity of the Oldroyd-B equation (non-zero $N_1$) explains the increase in the magnitude of the viscoelastic normal stress while the viscous normal stress which is proportional to local strain rate, does not show any significant change.

Next, we look at the stresses tangential to the drop interface (i.e. along the streamlines/path lines). In figure 6(*c*), we see that the viscous tangential stresses (like the viscous normal stresses) do not show significant variation with *De*. The viscoelastic tangential stresses (figure 6*d*), however, show a marked increase in magnitude with increasing *De*. The viscous and the viscoelastic tangential stresses are both tensile near the equator of the drop. Along curved streamlines, the 'extra' viscoelastic tensile stress gives rise to a *hoop stress* effect, exerting a net inward pull on the drop interface. This induces a higher pressure at the drop equator, thus pushing the drop outwards, as concluded by Yue *et al.* (2005*a*). To summarize, the viscoelastic normal stresses at the drop tips and the viscoelastic tangential stresses at the drop equator are responsible for a reduction in drop deformation with increasing *De*.
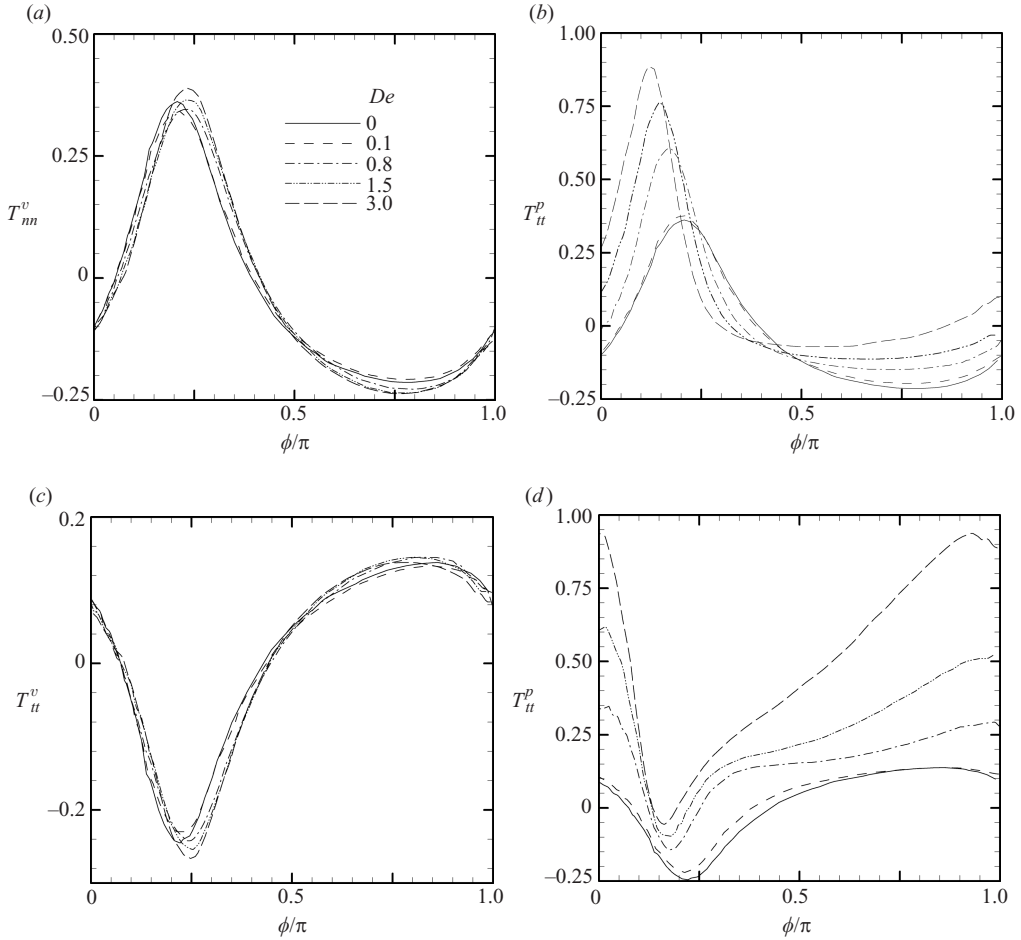
FIGURE 6. Stresses along the circumference of the drop in the $z = L_z/2$ plane plotted as a function of the angular position ($\phi = 0$ coincides with the $x$-axis) for different $De$ at $Ca = 0.2$. Because of the symmetry, only half of the drop is shown. (*a*) Viscous normal stresses $T_{nn}^v = \mathbf{n} \cdot \mathbf{T}^v \cdot \mathbf{n}$, where $\mathbf{n}$ is the outward normal to the circumference. (*b*) Viscoelastic normal stresses $T_{nn}^p = \mathbf{n} \cdot \mathbf{T}^p \cdot \mathbf{n}$ (*c*) Viscous tangential stresses $T_{tt}^v = \mathbf{t} \cdot \mathbf{T}^v \cdot \mathbf{t}$, where $\mathbf{t}$ is a vector in the $z = L_z/2$ plane, tangential to the circumference of the drop. (*d*) Viscoelastic tangential stresses $T_{tt}^p = \mathbf{t} \cdot \mathbf{T}^p \cdot \mathbf{t}$.

In figure 7(*b*), we plot the primary eigenvalue of the conformation tensor $\mathbf{A}(= (\lambda/\mu)\mathbf{T}^p + \mathbf{I})$ which indicates the orientation and stretch of the polymer molecules, at each node point in the viscoelastic phase. The orientation of the polymer molecules shown in figure 7*b* corroborates our observation about the trends in viscoelastic tangential and normal stresses at the interface. The polymer molecules are perpendicular to the interface near the drop tips, whereas they are tangential to the interface around the equator. We see that the respective stresses are significant at the corresponding angular positions. Note that a very similar plot was also obtained in the two-dimensional study by Yue *et al.* (2005*a*).

We investigate the overall three-dimensional nature of the problem by looking at the viscoelastic stress in a plane perpendicular ($x = L_x/2$) to the flow direction. In figure 8, we plot the viscoelastic normal stress on the interface $T_{nn}^p$ as a function of
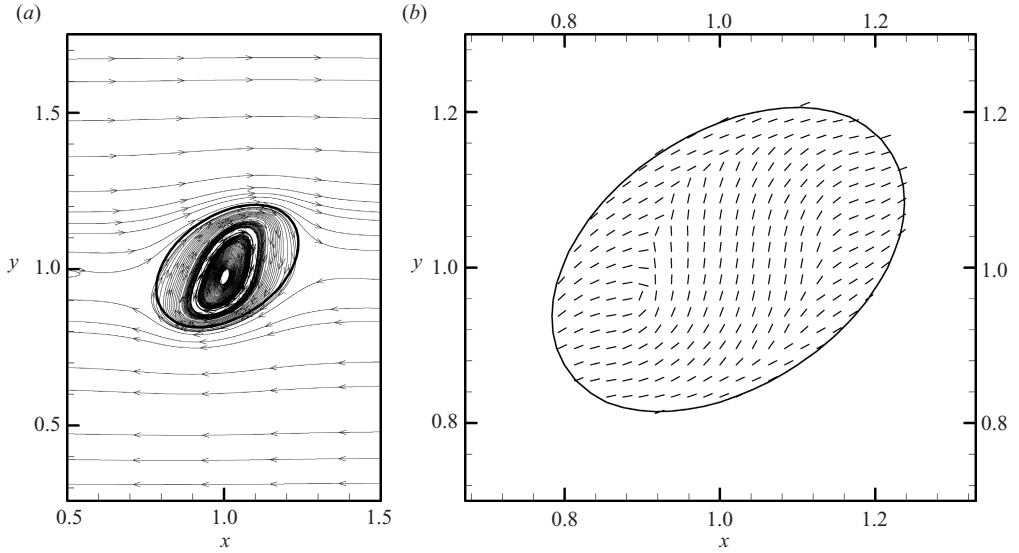
FIGURE 7. (*a*) Flow streamlines for a drop at steady state, in the $z = L_z/2$ plane at $Ca = 0.2$, $De = 2.0$. The density of the streamlines inside the drop has been manually varied to give a clearer picture of the streamline pattern. (*b*) Dominant polymer orientation at $Ca = 0.2$, $De = 2.0$ in the $z = L_z/2$ plane.
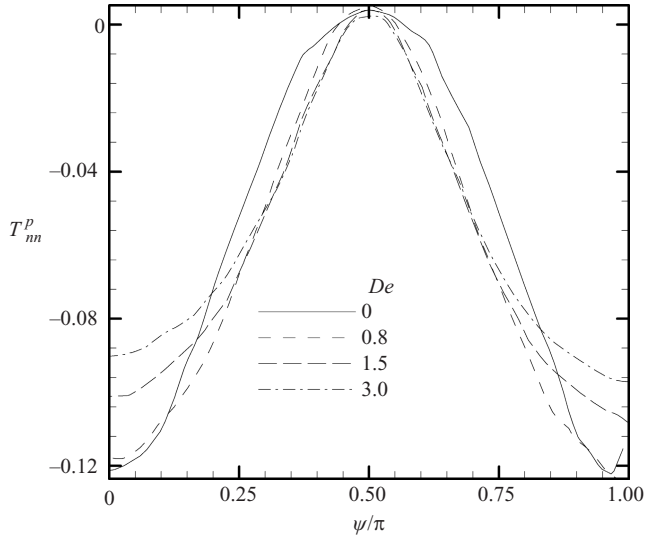


FIGURE 8. Viscoelastic normal stresses along the circumference of the drop in the $x = L_x/2$ plane *vs.* angular position ($\psi = 0$ coincides with $y$-axis) for different $De$ at $Ca = 0.2$.

the angular position $\psi$. The stress magnitude is much lower than that in the $z = L_z/2$ plane, because the polymer molecules are primarily oriented along the flow direction. The effect of viscoelasticity, albeit small, is examined for trends. In contrast to the trend in figure 6*b* the polymeric normal stresses in figure 8 are always negative, thus exerting a 'push' on the drop interface, trying to reduce $W$ (and $B$) axis deformations (figure 3*a*). Levitt & Macosko (1996) reported a widening of viscoelastic drops in the vorticity direction for a system with significant second normal stresses. Note that an
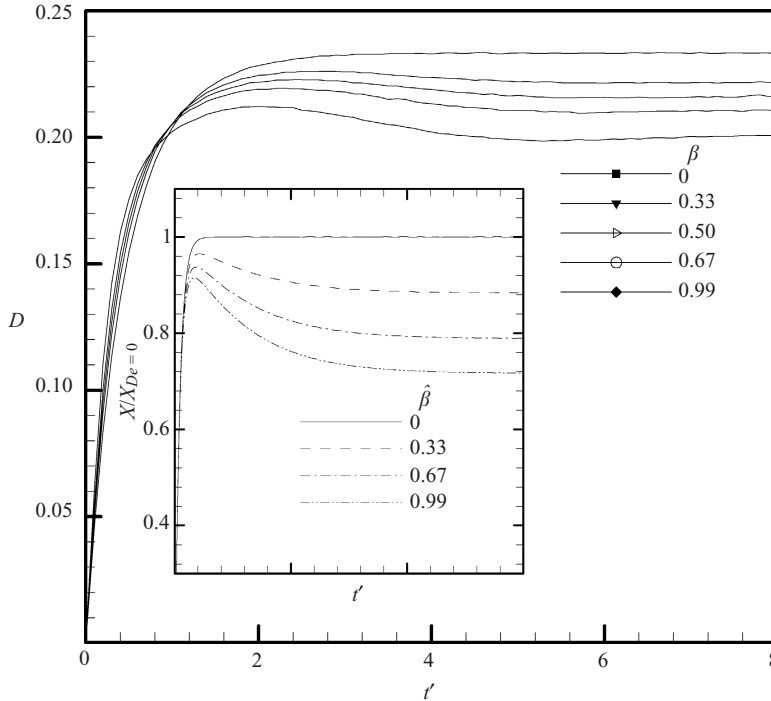
FIGURE 9. Transient drop deformation $D$ vs. $t'$ plotted for different viscosity ratios $\beta(= \mu_{pd}/\mu_d)$ at $Ca = 0.2$, $De = 2.0$. The inset shows drop response predictions of our ODE model $X$ for $\beta$ variations at $\hat{C}a = 0.2$, $\hat{D}e = 2$

Oldroyd-B fluid has a zero second normal stress difference. The tangential viscoelastic stress $T_{tt}^p$ in the same plane shows a small positive value (not shown here).

### 5.4. *Variation of parameter $\beta$*

Next we look at the effect of varying parameter $\beta(= \mu_{pd}/\mu_d)$, while keeping the viscosity ratio constant $\lambda\mu = (\mu_{pd} + \mu_{sd})/\mu_m = 1$. For $\beta = 1$, we obtain an upper convected Maxwell (UCM) constitutive equation for the drop phase. In figure 9, we plot the transient drop deformation for $Ca = 0.2$, $De = 2.0$ and varying $\beta$ values. We see no overshoots in the transient deformation for $\beta = 0$. However, on increasing $\beta$, not only do we see an overshoot, but the overshoot magnitude increases. The steady-state drop deformation decreases with increasing $\beta$. The inset of figure 9 shows predictions of our ODE model for $\hat{C}a = 0.2$, $\hat{D}e = 2$. Our model is able to capture the decrease in steady-state deformation as well as the increase in the magnitude of overshoot (difference between the maximum value during the transient deformation $D_{max}$ and $D_{st}$). Toose *et al.* (1995) concluded in their two-dimensional study that the effect of the parameter $\beta$ is evident only in the transient deformation, while the steady-state deformation remains unchanged. We would like to note that this is true only for $Ca \ll 1$, which was the focus of their study. On increasing $\beta$, we also see an increase in $\varphi$, i.e. a reduction in the drop alignment with the flow direction (figure 10). This reduced alignment is consistent with the observed reduction in steady-state deformation.

In figure 11, we plot $D_{st}$ and $D_{max}$ for $Ca = 0.2$ with varying $De$ as a function of $\beta$ (no plot for $D_{max}$ for $De = 0.25$ as there is no overshoot for this Deborah number
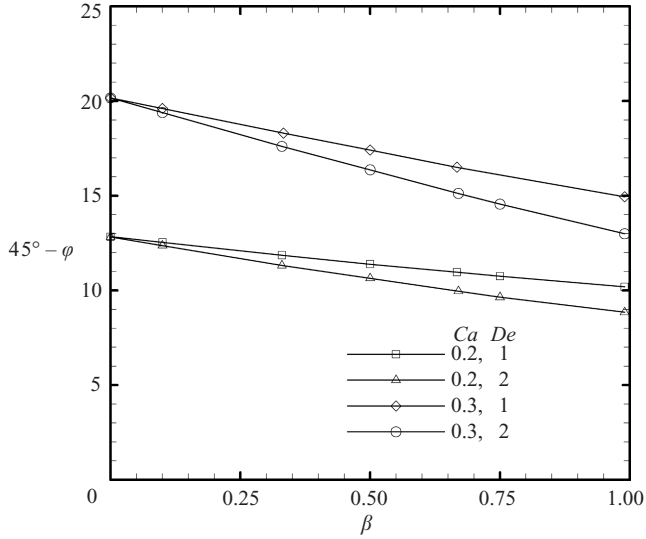
FIGURE 10. Variation of steady-state drop inclination angle $\varphi$ from the strain-rate axis,
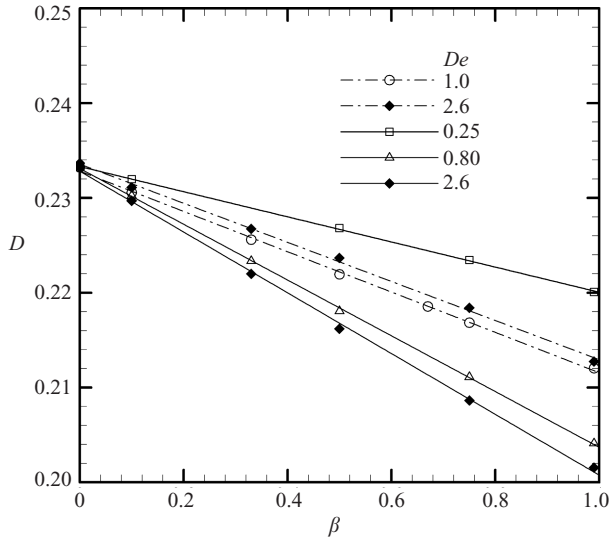$45° - \varphi$ with $\beta$.



FIGURE 11. Drop deformation parameter $D$ plotted *vs.* $\beta$ for varying $De$ at $Ca = 0.2$. Solid
lines represent a linear fit over the steady state deformation values $D_{st}$. Dash-dotted lines
represent a linear fit over the maximum value of deformation $D_{max}$.

for any $\beta$). We see a decrease in $D_{st}$ and $D_{max}$ with increasing $\beta$. The magnitude of
overshoot $D_{max} - D_{st}$, increases with both $\beta$ and $De$. An increase in $\beta$, for constant
$De$, is equivalent to increasing the viscoelastic contributions in the drop phase. A
linear least-squares curve fits the data sets very well. This linear decrease of $D_{st}$ with
$\beta$ is also predicted by our ODE model (see (19)). The slope of the linear fit changes
with $De$; however, the effect of $De$ variation saturates as noted previously (figure 4*b*).
Note the negligible difference between the $De = 0.8$ and $De = 2.6$ curves.

In figure 12, we look at plots of viscous and viscoelastic stresses, normal to the
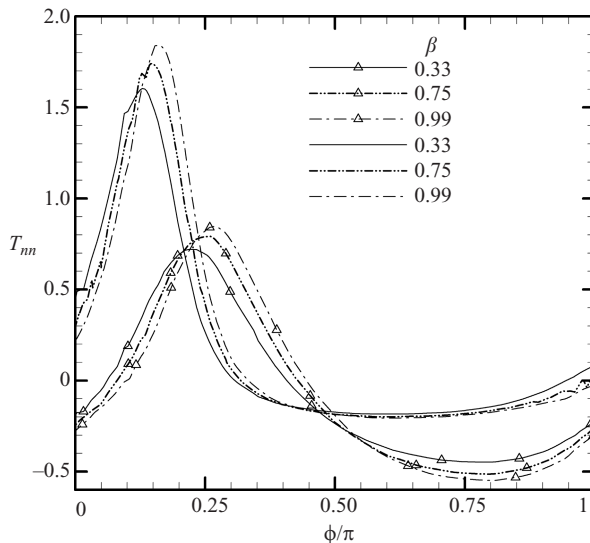drop circumference (similar to figure 6*a, b*) for $Ca = 0.2$, $De = 2.0$ and varying $\beta$. We

FIGURE 12. Viscous ($T_{nn}^v$) and Viscoelastic ($T_{nn}^p$) normal stresses (normalized with $\mu_{sd}\dot{\gamma}$ and $\mu_{pd}\dot{\gamma}$, respectively) along the drop circumference in the $z = L_z/2$ plane *vs.* angular position from the $x$-axis. Curves with symbols represent viscous normal stresses. Curves are for parameter values $Ca = 0.2$, $De = 2.0$ and varying $\beta$.

see that the magnitudes of the stresses do change with $\beta$. However, in contrast to figure 6(a, b), the angular phase lag between the peak values of the viscous and the viscoelastic stresses does not change significantly for the different $\beta$ values. This is because the relaxation time ($De$) is the same for all cases.

## 5.5. *Critical capillary numbers*

Drop elasticity inhibits drop deformation. Hence, we expect the critical capillary number $Ca_{cr}$ for a viscoelastic drop to increase from the Newtonian case. Use of numerical methods for determination of $Ca_{cr}$ is fraught with convergence issues. As reported by Li & Sarkar (2006), it becomes difficult to obtain grid convergence close to the critical parameter set. A parameter set predicting drop breakup at a particular resolution might result in a steady shape on grid refinement. Hence, the critical parameters can be estimated only within a certain error-bound. The lower bound refers to the maximum $Ca$ (for a particular $De$) for which we see a bounded shape even with grid refinement. Similarly, the upper bound refers to the minimum $Ca$ for which we obtain unbounded drops with grid refinement. In contrast to the drop breakup study for viscous drops in a vortex flow (Li & Sarkar 2006), whether a viscoelastic drop in a sheared matrix eventually breaks up, is not easily ascertained close to the critical case owing to the long time scale of the process. Hence, lengthy computations must be performed to determine the critical parameters precisely. We have thus chosen to present in our study, only the lower bounds for most of the data points. In figure 13, we plot drop deformation parameter $L/a$ ($L/a$ is a more appropriate representation of large deformations; Bentley & Leal 1986) for $Ca = 0.45$. We see that for $De = 1.4$, we obtain a bounded drop shape at a grid resolution of $96 \times 96 \times 48$. On using a finer mesh ($112 \times 112 \times 56$), the drop still attains a bounded drop shape. On increasing the capillary number to $Ca = 0.47$ while keeping $De = 1.4$, we see unbounded drop shapes for both grid resolutions. Hence, we deduce $Ca = 0.47$ to be the upper bound at $De = 1.4$.
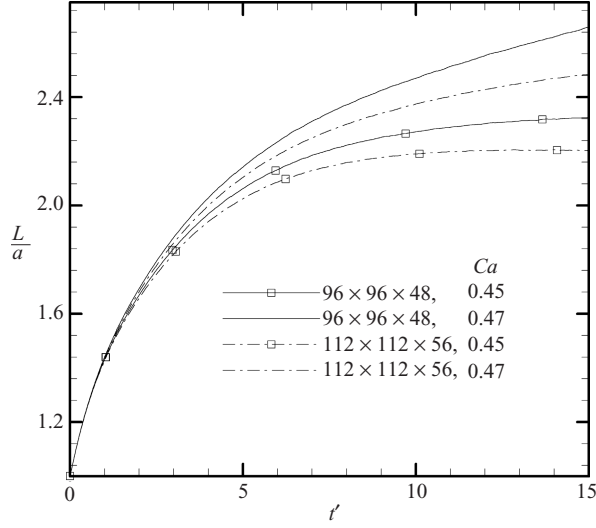
FIGURE 13. Drop deformation predictions $L/a$ for parameters close to the critical case at grid resolutions of $96 \times 96 \times 48$ and $112 \times 112 \times 56$.
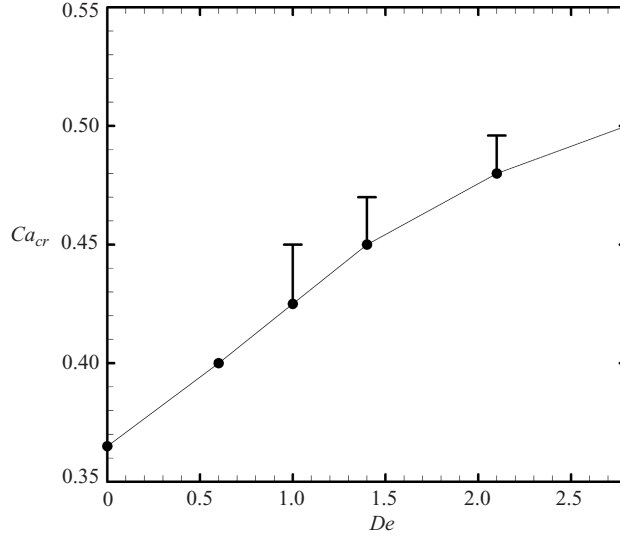


FIGURE 14. Effect of $De$ variation on critical capillary numbers $Ca_{cr}$ at viscosity ratio $\lambda_\mu = 1$ in simple shear flow. Upper bounds are indicated in $Ca$ and are determined for $De = 1$, $De = 1.4$ and $De = 2.1$.

In figure 14, we compute the $Ca_{cr} \sim De$ curve for a fixed viscosity ratio $\lambda_\mu = 1$, (and $\beta = 0.5$). Our numerical simulations are performed at small but finite $Re = 0.1$. The critical capillary number for the Newtonian case ($De = 0$) is found to be $Ca_{cr} = 0.365$. Renardy & Cristini (2001) in their numerical study using a volume-of-fluid (VOF) method, determined the critical capillary number at $Re = 0.1$ and $\lambda_\mu = 1$ to be $\approx 0.38$. The curve increases monotonically as expected because of inhibitive viscoelastic stress in the drop phase. Moreover, the curve is linear for small $De$. Linear dependence of $Ca_{cr}$ on $De$ was also observed by Lerdwijitjarud et al. (2003) in their experimental

study. A quantitative match with their results is not possible because the matrix phase in their study is also non-Newtonian and shows both shear thinning and elastic effects.

The mode of breakup for viscoelastic drops could be significantly different from that of Newtonian drops. A viscoelastic drop undergoes a significant amount of stretching over a long period of time (Varanasi *et al.* 1994), a detailed study of which remains beyond the scope of the present investigation. .

## 6. Summary

In this study, drop deformation and breakup of a viscoelastic (Oldroyd-B) drop suspended in a Newtonian matrix, subjected to a simple shear flow, have been investigated using a three-dimensional front-tracking algorithm. We observe that drop viscoelasticity tends to inhibit drop deformation $D$ in agreement with previous experimental and numerical studies. The drop deformation decreases with $De$ owing to extra viscoelastic stresses inside the drop; the evolution in deformation shows an overshoot in time owing to finite relaxation time for the development of viscoelastic stresses, and the drop shows slightly decreased alignment with the imposed flow. However, at high $Ca$, the steady deformation experiences a slight increase with increasing $De$; the initial deformation is too high to be countered by the eventual buildup of viscoelastic stresses. We analyse the normal forces at the drop interface to show conclusively the inhibiting effects of viscoelastic stresses on drop deformation. Our results match well with the ellipsoidal drop model theory of Maffetone & Greco (2004) for small deformation. We also investigate in detail the effects of varying polymer and solution viscosities keeping the relaxation time the same. We have developed a simple force balance ODE model that provides a qualitative description for all our observations. It predicts the observed scaling $D/D_{De=0} \sim DeCa$. The ODE model is also able to show clearly how overshoots in transient drop deformation can be explained by the relaxation behaviour of our rate-type constitutive equation. The observed drop response with $\beta$ variation is also captured by the model. Finally, we perform a study of breakup of a viscoelastic drop to note that the critical capillary number increases with elasticity with $Ca_{cr} \sim De$ for small $De$.

## REFERENCES

BARTHÈS-BIESEL, D. & ACRIVOS, A. 1973 Deformation and burst of liquid droplet freely suspended in a linear shear field. *J. Fluid Mech.* **61**, 1–21.

BENTLEY, B. J. & LEAL, L. G. 1986 An experimental investigation of drop deformation and breakup in steady, two-dimensional linear flows. *J. Fluid Mech.* **167**, 241–283.

DE BRUIJN, R. A. 1989 Deformation and breakup of droplets in simple shear flows. PhD thesis, Eindhoven University of Technology, Eindhoven, The Netherlands.

CHAFFEY, C. E. & BRENNER, H. 1967 A second-order theory for shear deformation of drops. *J. Colloid Interface Sci.* **24**, 258–269.

GAUTHIER, F., GOLDSMITH, H. L. & MASON, S. G. 1971 Particle motions in non-Newtonian media. II: Poiseuille flow. *Trans. Soc. Rheol.* **15**, 297–330.

GRACE, H. P. 1982 Dispersion phenomena in high viscosity immiscible fluid systems and application of static mixers as dispersion devices in such systems. *Chem. Engng Commun.* **14**, 225–277.

GRECO, F. 2002 Drop deformation for non-Newtonian fluids in slow flows. *J. Non-Newtonian Fluid Mech.* **107**, 111–131.

GUIDO, S., SIMEONE, M. & GRECO, F. 2003 Deformation of a Newtonian drop in a viscoelastic matrix under steady shear flow: experimental validation of slow flow theory. *J. Non-Newtonian Fluid Mech.* **114**, 65–82.

HOOPER, R. W., DE ALMEDIA, V. F., MACOSKO, C. W. & DERBY, J. J. 2001 Transient polymeric drop extension and retraction in uniaxial extensional flows. *J. Non-Newtonian Fluid Mech.* **98**, 141–168.

KHISMATULLIN, D., RENARDY, Y. & RENARDY, M. 2006 Development and implementation of VOF-PROST for 3D viscoelastic liquid–liquid simulations. *J. Non-Newtonian Fluid Mech.* **140**, 120–131.

LERDWIJITJARUD, W., LARSON, R. G., SIRIVAT, A. & SOLOMON, M. J. 2003 Influence of weak elasticity of dispersed phase on droplet behavior in sheared polybutadiene/poly(dimethyl siloxane) blends. *J. Rheol.* **47** (1), 37–58.

LEVITT, L. & MACOSKO, C. W. 1996 Influence of normal stress difference on polymer drop deformation. *Polymer Engng Sci.* **36**, 1647–1655.

LI, X. & SARKAR, K. 2005*a* Drop dynamics in an oscillating extensional flow at finite inertia. *Phys. Fluids* **17**, 027103.

LI, X. & SARKAR, K. 2005*b* Rheology of a dilute emulsion of drops in finite Reynolds number oscillator extensional flows. *J. Non-Newtonian Fluid Mech.* **128**, 71–82.

LI, X. & SARKAR, K. 2005*c* Effects of inertia on the rheology of a dilute emulsion of drops in shear. *J. Rheol.* **49**, 1377–1394.

LI, X. & SARKAR, K. 2005*d* Negative normal stress elasticity of emulsion of viscous drops at finite inertia. *Phys. Rev. Lett.* **95**, 256001.

LI, X. & SARKAR, K. 2006 Drop deformation and breakup in a vortex for finite inertia. *J. Fluid Mech.* **564**, 1–23.

MAFFETONE, P. L. & GRECO, F. 2004 Ellipsoidal drop model for single drop dynamics with non-Newtonian fluids. *J. Rheol.* **48**, 83–100.

MAFFETONE, P. L. & MINALE, M. 1998 Equation of change for ellipsoidal drops in viscous flow. *J. Non-Newtonian Fluid Mech.* **78**, 227–241.

MIGHRI, F. A., CARREAU, P. J. & AJJI, A. 1998 Influence of elastic properties on drop deformation and breakup in shear flow. *J. Rheol.* **42**, 1477–1490.

MIGHRI, F. A., AJJI, A. & CARREAU, P. J. 1997 Influence of elastic properties on drop deformation in elongational flow. *J. Rheol.* **41**, 1183–1201.

PERERA, M. G. N. & WALTERS, K. 1977 Long-range memory effects in flows involving abrupt changes in geometry part I: flows associated with L-shaped and T-shaped geometries. *J. Non-Newtonian Fluid Mech.* **2**, 49–81.

PESKIN, C. 1977 Numerical analysis of blood flow in the heart. *J. Comput Phys.* **25**, 220–252.

PILAPAKKAM, S. B. & SINGH, P. 2004 A level-set method for computing solutions to viscoelastic two-phase flow. *J. Comput. Phys.* **174**, 552–578.

RAJAGOPALAN, D., ARMSTRONG, R. C. & BROWN, R. A. 1990 Finite element methods for calculations of steady, viscoelastic flow using constitutive equations with a Newtonian viscosity. *J. Non-Newtonian Fluid Mech.* **36**, 159–192.

RALLISON, J. M. 1984 The deformation of small viscous drops and bubbles in shear flows. *Annu. Rev. Fluid Mech.* **16**, 45–66.

RALLISON, J. M. & HINCH, E. J. 1988 Do we understand the physics in the constitutive equation? *J. Fluid Mech.* **29**, 37–55.

RAMASWAMY, S. & LEAL, L. G. 1999*a* The deformation of a viscoelastic drop subjected to steady uniaxial extensional flow of a Newtonian fluid. *J. Non-Newtonian Fluid Mech.* **85**, 127–163.

RAMASWAMY, S. & LEAL, L. G. 1999*b* The deformation of a Newtonian drop in the uniaxial extensional flow of a viscoelastic liquid. *J. Non-Newtonian Fluid Mech.* **88**, 149–172.

RENARDY, Y. & CRISTINI, V. 2001 Effects of inertia on drop breakup under shear. *Phys. Fluids* **13**, 7–13.

SARKAR, K. & SCHOWALTER, W. R. 2000 Deformation of a two-dimensional viscoelastic drop at non-zero Reynolds number in time-periodic extensional flows. *J. Non-Newtonian Fluid Mech.* **95**, 315–342.

SARKAR, K. & SCHOWALTER, W. R. 2001*a* Deformation of a two-dimensional drop at non-zero Reynolds number in time-periodic extensional flows: numerical simulation. *J. Fluid Mech.* **436**, 177–206.

SARKAR, K. & SCHOWALTER, W. R. 2001*b* Deformation of a two-dimensional viscous drop time-periodic extensional flows: analytical treatment. *J. Fluid Mech.* **436**, 207–230.

SIBILLO, V., SIMEONE, M. & GUIDO, S. 2004 Break-up of a Newtonian drop in a viscoelastic matrix under simple shear flow. *Rheol. Acta.* **43**, 449–456.

STONE, H. A. 1994 Dynamics of drop deformation and breakup in viscous fluids. *Annu. Rev. Fluid Mech.* **26**, 65–102.

SUN, J. & TANNER, R. I. 1994 Computation of steady flow past a sphere in a tube using a PTT integral model. *J. Non-Newtonian Fluid Mech.* **54**, 379–403.

SUN, J., PHAN-THIEN, N. & TANNER, R. I. 1996 An adaptive viscoelastic stress splitting scheme and its applications: AVSS/SI and AVSS/SUPG. *J. Non-Newtonian Fluid Mech.* **65**, 75–91.

TAYLOR, G. I. 1932 The viscosity of a fluid containing small drops of another fluid. *Proc. R. Soc. Lond.* A **138**, 41–48.

TAYLOR, G. I. 1934 The formation of emulsions in definable fields of flow. *Proc. R. Soc. Lond.* A **146**, 501–523.

TOOSE, E. M., GUERTS, B. J. & KUERTEN, J. G. M. 1995 A boundary integral method for two-dimensional (non)-Newtonian drops in slow viscous flow. *J. Non-Newtonian Fluid Mech.* **60**, 129–154.

TORZA, S., COZ, R. G. & MASON, S. G. 1972 Particle motions in sheared suspensions XXVII. Transient and steady deformation and burst of liquid drops. *J. Colloid Interface Sci.* **38**, 395–411.

TRYGGVASON, G., BUNNER, B., EBRAT, O. & TAUBAR, W. 1998 Computation of multiphase flows by a finite difference front tracking method. I. Multi-fluid flows. *29th Computational Fluid Dynamics Lecture Series* 1998–2003. Von Kármán Institute of Fluid Dynamics, Sint-Genesius-Rode, Belgium.

TRYGGVASON, G., BUNNER, B., ESMAEELI, A., JURIC, D., AL-RAWAHI, N., TAUBAR, W., HAN, J., NAS, S. & JAN, Y. J. 2001 A front-tracking method for computations of multiphase flow. *J. Comput Phys.* **169**, 708–759.

TUCKER III, C. L. & MOLDENAERS, P. 2002 Microstructural evolution in polymer blends. *Annu. Rev. Fluid Mech.* **34**, 177–210.

UNVERDI, S. O. & TRYGGVASON, G 1992 A front-tracking method for viscous, incompressible multi-fluid flows. *J. Comput. Phys.* **100**, 25–37.

VARANASI, P. P., RYAN, M. E. & STROEVE, P. 1994 Experimental study on the breakup of model viscoelastic drops in uniform shear flow. *Ind. Engng Chem. Res.* **33**, 1858–1866.

YU, W., BOUSMINA, M., ZHOU, C. & TUCKER III, C. L. 2004 Theory for drop deformation in viscoelastic systems. *J. Rheol.* **48**, 417–438.

YUE, P., FENG, J. J., LIU, C. & SHEN, J. 2005*a* Viscoelastic effects on drop deformation in steady shear. *J. Fluid Mech.* **540**, 427–437.

YUE, P., FENG, J. J., LIU, C. & SHEN, J. 2005*b* Transient drop deformation upon start up shear in viscoelastic fluids. *Phys. Fluids* **17**, 123101.